ANNUAL REVIEWS

*Annual Review of Nuclear and Particle Science*

# Double-Higgs Production

Loukas Gouskos[1] and Katharine J.C. Leney[2]

[1]Department of Physics, Brown University, Providence, Rhode Island, USA; email: loukas.gouskos@cern.ch

[2]Department of Physics, Southern Methodist University, Dallas, Texas, USA



Annu. Rev. Nucl. Part. Sci. 2024. 74:263–86

First published as a Review in Advance on July 1, 2024

The *Annual Review of Nuclear and Particle Science* is online at nucl.annualreviews.org

https://doi.org/10.1146/annurev-nucl-102622-014457



## Keywords

Higgs, Higgs self-coupling, Higgs boson pair production

## Abstract

A major focus in particle physics has been on understanding the interactions of the Higgs boson. Tremendous progress has been made in determining the strength of the couplings of the Higgs boson to fermions and vector bosons, but its self-interaction has yet to be established. Understanding the Higgs self-coupling and the form of the potential function of the Higgs field will illuminate the process by which the Higgs boson acquires a vacuum expectation value and could provide insight into the early Universe and, perhaps, its eventual fate. The most natural way to probe the Higgs self-interaction is via searches for Higgs boson pair (*HH*) production. Since the Standard Model makes a definite prediction for the Higgs self-coupling, enhanced rates and modified kinematic properties of *HH* production are a smoking-gun signature for new physics. This article reviews the current experimental status of *HH* searches, discusses the experimental challenges and limitations, and provides an outlook for the future of the field.

## Contents



## 1. INTRODUCTION

The Standard Model (SM) of particle physics stands as the cornerstone in our understanding of the fundamental building blocks of the Universe. Central to the SM is the Brout–Englert–Higgs (BEH) mechanism (1–3), which introduces a scalar field whose manifestation is the Higgs boson. This field permeates the entire Universe, imparting mass to fundamental particles through its interaction with the particles. This groundbreaking theoretical idea, proposed in 1964, was confirmed experimentally almost 50 years later, in 2012, with the discovery of the Higgs boson.

This seminal discovery was the result of a monumental effort by more than 5,000 scientists from around the world who collaborated on rigorous experimental undertakings and sophisticated analyses using data collected by the ATLAS (4) and CMS (5) experiments at CERN's Large Hadron Collider (LHC). The LHC accelerates protons to energies never before achieved by humankind, before colliding them at the heart of the detectors. These collisions emulate conditions akin to those prevailing in the Universe shortly after the Big Bang.

The discovery of the Higgs boson was a paradigm-shifting moment that solidified our understanding of the basic building blocks of the Universe. The Higgs boson was first observed via its direct couplings to the vector ($V$) bosons, $W$ and $Z$, and its effective coupling to photons (6, 7). In the decade following this discovery, scientists made significant progress in unraveling the intricacies of the BEH mechanism. A major milestone in understanding the Higgs boson involves understanding its interactions with fermions. Interactions between the Higgs field and fermions are particularly important because they are not predicted by the BEH mechanism, as fermions acquire mass via a Yukawa interaction, or coupling, with the Higgs field. Such couplings are free

parameters that need to be measured experimentally. Understanding the precise values of these couplings is crucial, as any deviation from the expected values would point to new, unanticipated physics beyond the SM (BSM). Interactions between the Higgs boson and third-generation fermions—tau ($\tau$) leptons, bottom ($b$) quarks, and top ($t$) quarks—have been experimentally verified (8–13) and so far have been consistent with SM predictions.

The next steps in understanding these fermionic interactions are to observe and measure decays to second-generation fermions. Evidence of the Higgs boson decaying to a pair of muons has been established by the ATLAS (14) and CMS (15) Collaborations using the data collected during the second run of the LHC (Run 2). Establishing interactions with second-generation quarks will be extremely challenging; until very recently, it was thought to be impossible to do so at a hadron collider. However, recent advancements in object reconstruction and in analysis techniques offer the hope to probe the interactions between the Higgs boson and charm ($c$) quarks (14, 15) at the High Luminosity LHC (HL-LHC). Probing interactions between the Higgs boson and the first-generation fermions is even more challenging, given the mass dependence of the Higgs boson's couplings. The current best limit on the branching fraction for Higgs boson decays to a pair of electrons, set by the CMS Collaboration (16), is $3.0 \times 10^{-4}$, but this value is still five orders of magnitude larger than the SM value of $\mathrm{BR}(H \to e^+e^-) \sim 10^{-9}$. This decay mode will almost certainly remain out of reach at the HL-LHC and will be accessible only at future collider experiments.

Despite this progress, many more characteristics of the Higgs boson remain to be explored. Arguably, the ultimate goal is to understand the shape of the potential of the Higgs field. In the context of mass terms, the Higgs potential dictates which particles obtain mass, as well as the magnitude of that mass. It explains why certain particles are heavier than others and shapes our physical world. Furthermore, the potential's higher-order terms, specifically the third- and fourth-order terms, play a subtle yet vital role in refining our understanding of the Universe at the quantum level.

The most direct way to access higher-order terms of the Higgs potential is by searching for multiple Higgs boson production. For instance, Higgs boson pair ($HH$) production provides information about how the Higgs boson interacts with itself. The strength of the Higgs boson's self-coupling ($\lambda_{HHH}$) is an exact prediction of the SM that can be inferred from the Higgs boson mass ($m_H$) and vacuum expectation value ($v$) using the formula $m_H^2 = 2\lambda_{HHH}v^2$. This relationship gives rise to interactions involving three and four Higgs bosons after the electroweak (EW) symmetry is broken spontaneously.

The nature of the EW phase transition, when the electromagnetic and weak forces differentiated as the Universe cooled down after the Big Bang, is still unknown. Observing and measuring $HH$ production, and eventually triple-Higgs ($HHH$) production, are key to verifying the nature of EW symmetry breaking. The SM predicts a graceful crossover from one phase to the other, but most models need a violent first-order phase transition in order to accommodate phenomena like baryogenesis. New physics that interacts with the Higgs boson is required to accommodate a first-order phase transition, which in turn leads to a large (of order one) modification to the Higgs self-coupling (17, 18). Some models of inflation (19, 20) require that the Higgs boson couple to gravity, thereby modifying the shape of the Higgs potential. Measurements of $\lambda_{HHH}$ can provide important information to constrain these models, can place constraints on cosmological phenomena such as the reheat temperature and the scale of inflation, and may even offer clues about the eventual fate of the Universe (21). Models of EW baryogenesis typically predict deviations of $\lambda_{HHH}$ in the range 25–50% (22) of the SM prediction. At a precision approaching 10%, the measurements will be sensitive to a broad class of loop diagram effects, such as those that might be produced by light top squarks (22).

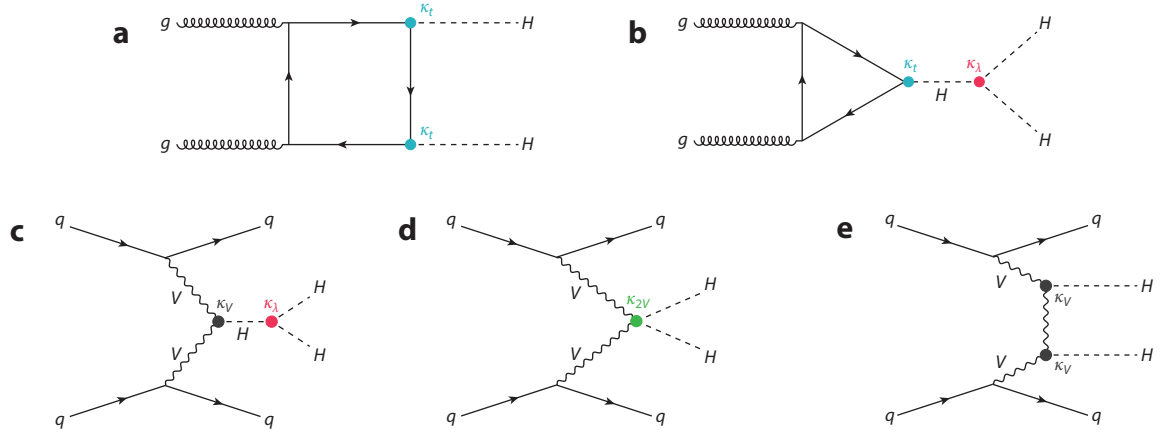


**Figure 1**

Leading-order diagrams for gluon–gluon fusion *HH* production via (*a*) a box loop and (*b*) the self-interaction triangle mode. The *ttH* and *HHH* vertices are indicated by turquoise and dark pink dots on the diagrams, and the coupling strength modifiers are denoted as $\kappa_t$ and $\kappa_\lambda$, respectively. Leading-order processes contributing to VBF *HH* production, with diagrams containing (*c*) the *HHH* and *VVH* couplings ($\kappa_V$; *black dot*), (*d*) the quartic *VVHH* coupling ($\kappa_{2V}$; *green dot*), and (*e*) the *VVH* coupling. Figure adapted from Reference 99 (CC BY 4.0).

This article provides a comprehensive overview of the field of *HH* physics. In Section 2, we present a theoretical overview of *HH* production. Section 3 describes the experimental techniques developed to measure *HH* production, followed in Section 4 by a survey of the current *HH* searches at the LHC and our understanding of the Higgs self-coupling. Finally, we touch on the challenges facing *HH* measurements and what the future might hold for *HH* physics in Section 5, and we present our conclusions in Section 6.

## 2. THEORETICAL OVERVIEW OF HIGGS BOSON PAIR PRODUCTION

### 2.1. Nonresonant Higgs Pair Production

The most direct way to probe the Higgs self-interaction is via *HH* production. At the LHC, the dominant *HH* production mode in the SM is via gluon–gluon fusion (*gg*F), either via a box loop of *t* quarks that is sensitive only to the coupling between the Higgs boson and *t* quarks, $\kappa_t$, or via the Higgs self-interaction (i.e., the triangle diagram), as shown at leading order (LO) in **Figure 1*a*** and ***b***, respectively. These two different *gg*F *HH* production modes interfere with each other destructively in the SM. This destructive interference contributes to a small cross section of only 31.05 fb for the *gg*F *HH* production process at $\sqrt{13}$ TeV, computed at next-to-next-to-leading order (NNLO) and including finite *t* quark mass effects (23–29).

Depending on the strength of the Higgs self-coupling relative to the SM prediction (denoted as $\kappa_\lambda = \lambda_{HHH}/\lambda_{HHH}^{\mathrm{SM}}$), the cross section of the $pp \rightarrow HH$ process and the shape of the $m_{HH}$ distribution change. Negative values of $\kappa_\lambda$ lead to constructive interference between the box (**Figure 1*a***) and triangle (**Figure 1*b***) diagrams, and the *HH* cross section is enhanced. For positive values of $\kappa_\lambda$ destructive interference occurs, leading to a deficit in the region between twice the Higgs boson mass and twice the *t* quark mass. The destructive interference is maximal around $\kappa_\lambda = 2$. The value $\kappa_\lambda = 0$ corresponds to the scenario where the diagram in **Figure 1*a*** does not exist, while for values of $\kappa_\lambda > 10$, the triangle diagram dominates. The $m_{HH}$ distribution is softest when $\kappa_\lambda = 5$, where the interference effects are less pronounced than at $\kappa_\lambda = 2$, but

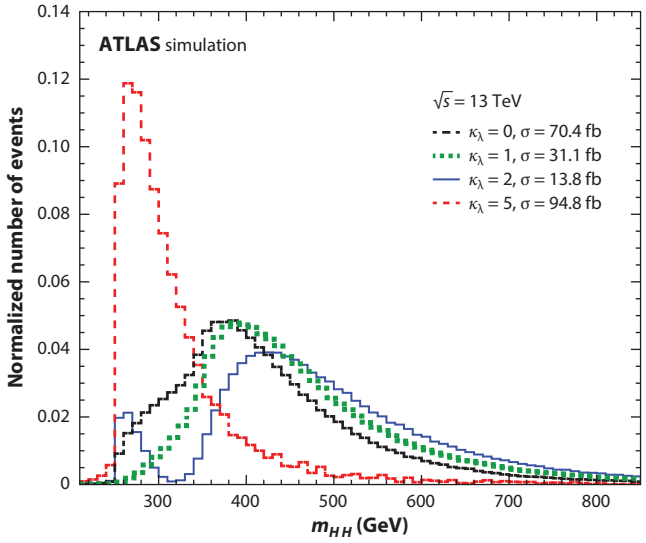


**Figure 2**

Generator-level $m_{HH}$ distributions computed for various values of $\kappa_\lambda$. The shape of the $m_{HH}$ distribution is determined by the interference between the box and triangle diagrams shown in **Figure 1*a*** and ***b***, respectively. For $\kappa_\lambda = 10$, the triangle diagram dominates the total production; in the $\kappa_\lambda = 0$ scenario, the triangle diagram does not contribute at all. The two diagrams maximally interfere at $\kappa_\lambda = 2$, leading to a deficit in the region between twice the Higgs mass and twice the $t$ quark mass. The distributions are normalized to the number of entries and do not show the effect on the cross section of varying $\kappa_\lambda$. Figure adapted from Reference 30 (supplementary material) (CC BY 4.0).

the interference at higher $m_{HH}$ values leads to a narrower $m_{HH}$ distribution. **Figure 2** shows the distributions of $m_{HH}$ for selected values of $\kappa_\lambda$. Maximizing analysis sensitivity in low-$m_{HH}$ regions is critical for constraining $\kappa_\lambda$ effectively but presents a challenge experimentally.

Vector boson fusion (VBF) *HH* production can be used to help measure the Higgs self-coupling, but more importantly it provides a way to probe the quartic *VVHH* coupling, $\kappa_{2V}$. **Figure 1*c*–*e*** depicts the LO Feynman diagrams contributing to VBF *HH* production. **Figure 1*c*** and ***d*** displays the diagrams whose amplitude depends on $\kappa_\lambda$ and $\kappa_{2V}$, respectively, whereas **Figure 1*e*** displays the diagram whose amplitude depends on the coupling of the Higgs boson with a $V$ boson, $\kappa_V$.

*HH* production in association with a $V$ boson (*VHH*) and in association with a pair of $t$ quarks ($t\bar{t}HH$) has a cross section of 0.87 fb and 0.78 fb, respectively, at a center-of-mass collision energy ($\sqrt{s}$) of 13 TeV. In theory the *VHH* production mode can resolve the *WWHH* and *ZZHH* couplings and constrain them separately, but in practice—once the fact that these are an order of magnitude less sensitive than the inclusive *VVHH* constraints is taken into account, and given the constraints on *WWH* and *ZZH* production from single-Higgs measurements—it is not clear that the current experimental constraints on the *WWHH* ($\kappa_{2W}$) and *ZZHH* ($\kappa_{2Z}$) couplings (31, 32) probe a physically allowed region.

## 2.2. Theoretical Uncertainties on Higgs Boson Pair Production

Theoretical uncertainties on *gg*F *HH* production are dominated by the finite order of the quantum chromodynamics calculation (+2.2%/–5% for $m_H = 125$ GeV and $\sqrt{s} = 13$ TeV) and by the choice of renormalization scheme and scale of the $t$ quark mass (+4%/–18%) (29, 33).

The renormalization of the $t$ quark mass affects the strength of the $t$ quark–Higgs coupling, a key factor in $HH$ production that affects both the production cross section and the $m_{HH}$ shape. Uncertainties in the strong coupling constant and parton distribution functions are also taken into account and have a combined effect of $\pm 3.0\%$ on the cross-section calculations.

A new Monte Carlo generator implementation for next-to-leading-order (NLO) $gg$F $HH$ processes (34) uses analytic results for the two-loop virtual corrections with the full $t$ quark mass dependence. It also provides more flexibility in the input parameters for event generation, including, for the first time, the possibility of varying the choice of $t$ quark mass renormalization scheme. This implementation will be used in LHC Run 3 analyses.

This new generator implementation also fixes a problem recently identified in the previous generator, where a missing term related to triangle diagrams affected predictions for BSM nonresonant $HH$ production (35). Note that this problem affects all $\kappa_\lambda$ limits and effective field theory (EFT) interpretations published by ATLAS and CMS that use the full LHC Run 2 data set. Differences of up to 35% have been noted (35), and the collaborations are still assessing their impact on the experimental results.

## 2.3. Indirect Probes of the Higgs Self-Coupling

Precise measurements of the cross section and decay width in single-Higgs production can also be used to place constraints on $\kappa_\lambda$ by exploiting the fact that single-Higgs production depends on $\kappa_\lambda$ via weak loops at NLO in the EW interactions (36–41). Not only does the inclusion of single-Higgs results provide additional constraints on $\kappa_\lambda$, but also the single-Higgs measurements are able to constrain the $ttH$ coupling strength, $\kappa_t$, and its sign (42), where the $HH$ measurements have little constraining power.

## 2.4. Higgs Boson Pair Production Beyond the Standard Model

While the discovery of the Higgs boson has completed the SM, several phenomena, including dark matter, the matter–antimatter asymmetry of the Universe, and gravity, remain unaccounted for. Furthermore, the presence of the Higgs boson introduces a hierarchy problem where radiative corrections to the Higgs mass must be extremely finely tuned to ensure that there is cancellation with the bare mass. Many theories that provide solutions to these open issues predict an enhancement of the nonresonant $HH$ production cross section or the existence of new particles that could decay to $HH$ and be accessible at the LHC. Such models include two-Higgs-doublet models (43), Kaluza–Klein excitations of Randall–Sundrum gravitons (44–46), composite Higgs models (47, 48), and pseudodilaton models (49).

$HH$ measurements can also provide complementary information about single-Higgs and EW precision observables in the context of EFT interpretations that allow new physics to be probed in a model-independent way. Global EFT fits that include inputs from single-Higgs and precision EW measurements are needed to constrain other operators and provide additional information on the Higgs self-coupling, while $HH$ measurements can provide a unique way to probe several BSM couplings, including the direct interactions between a pair of gluons or $t$ quarks and a pair of Higgs bosons ($ggHH$ and $ttHH$ vertices, respectively) that do not appear in single-Higgs processes at tree level.

Two main formalisms for EFTs are commonly used: the Higgs effective field theory (HEFT) (50, 51), where the Higgs field is an SU(2)×U(1) singlet, and the SM effective field theory (SMEFT) (52, 53), where the Higgs field is a component of an $SU(2)_L$ doublet field, $\phi$, as in the SM. The SMEFT formalism is motivated by the similarities between the masses of the Higgs and $V$ bosons, as well as by the absence of any direct discovery of new physics at the LHC;

in contrast, the HEFT formalism usually requires large deviations from the SM. SMEFT relates double- and single-Higgs couplings to other couplings that do not contain a Higgs boson and allows single-Higgs and EW precision measurements to constrain couplings of interest to *HH* measurements. At any given order of its expansions, SMEFT is typically more predictive than HEFT (22). Searches for (and, eventually, measurements of) *HH* processes can be used to set constraints on processes containing BSM *ggHH* and *ttHH* vertices—$c_{ggbb}$ and $c_{tt}$ in the HEFT formalism—that are not accessible at tree level via any other process.



## 3. EXPERIMENTAL TECHNIQUES

Observing and measuring *HH* production pose an additional set of challenges compared with single-Higgs production. The observation of the Higgs boson was driven by analyses targeting final states consisting of physics objects that can be efficiently and precisely reconstructed. The so-called golden channel involves examining events with four charged leptons resulting from the decays of a pair of $Z$ bosons produced by Higgs decay (54, 55). This channel provides the cleanest signature of all possible decay modes. The second most sensitive channel involved the search for Higgs bosons decaying into a pair of photons (via a loop-induced process) and searching for a narrow peak in the diphoton invariant mass ($m_{\gamma\gamma}$) distribution (56, 57). This analysis exploits the excellent energy resolution of photons but faces challenges from background originating from continuum production of two photons in association with jets.

These clean decay modes have very low branching ratios, like $H \to \gamma\gamma$ with a rate of $10^{-3}$. When applied to *HH* production, this decay mode results in a branching ratio of approximately $10^{-6}$. Since the cross section for *HH* production is more than three orders of magnitude smaller than that of single-Higgs production, searching for *HH* in such clean channels seems hopeless at the LHC and its future upgrades. Therefore, a practical approach involves exploring several decay modes that balance larger branching fractions and signal purity via better-reconstructed decay products. For the same reason, the collaborations also investigate different ranges of the momenta of the Higgs bosons thus produced as an additional way to improve the sensitivity. In parallel, substantial efforts have been dedicated to the reconstruction and identification of the Higgs boson decay products. Sections 3.1 and 3.2 delve into the key developments on these fronts. Techniques dedicated to specific analysis channels are presented in Section 4.

### 3.1. Fully Exploring Higgs Boson Decay Topologies

Traditionally, the approach to reconstructing Higgs boson decay products involves treating them as two distinct physics objects. For instance, in the case of Higgs boson decays to a pair of quarks, the particles from the hadronization of each quark are clustered using the anti-$k_T$ algorithm (58) with a distance parameter of 0.4, forming jets that we refer to below as small-$R$ jets. Both ATLAS and CMS use the same jet definition, and it is used to target resolved topologies where the Higgs boson decay products are resolvable as distinct objects.

Motivated by the increase in $\sqrt{s}$ at the LHC, which results in high-momentum objects, ATLAS and CMS began exploiting so-called boosted topologies. In this high-momentum regime, the resulting Higgs bosons have momenta considerably higher than their mass, leading to collimated decay products that are more efficiently reconstructed as a single jet, clustered with a larger distance parameter ($R = 1.0$ for ATLAS and $R = 0.8$ for CMS). Below, we refer to these as large-$R$ jets.

The boosted regime typically allows for better signal purity (and reduces combinatorial backgrounds), albeit with a trade-off of smaller signal acceptance, particularly in the low-$m_{HH}$ regime. While the use of large-$R$ jets enhances the reconstruction efficiency of high-momentum

objects, it introduces challenges such as susceptibility to effects of the underlying event and pileup contamination. Specific "grooming" algorithms (as in, e.g., 59, 60) are used to address these challenges. Grooming involves (*a*) reclustering jet constituents to filter out contributions from soft and wide-angle radiation and (*b*) mitigating pileup effects, which results in improvements in the reconstruction and identification of the Higgs boson candidates.

Experimentally, analyses probing nonresonant *HH* production in boosted topologies for *HH* physics have focused on the identification of $H \to b\bar{b}$ decays, a powerful tool in constraining $\kappa_{2V}$. Boosted topologies play an important role in searches for resonant *HH* production, where for high-mass resonances (>1 TeV) the Higgs bosons are produced at higher momenta.

Analyses exploring both resolved and boosted topologies are needed, as they provide complementary information for our understanding of the *HH* landscape. With the anticipated accumulation of more data during LHC Run 3 and more powerful artificial intelligence (AI) approaches to boosted object reconstruction, we expect an increased emphasis on boosted topologies in the next round of analyses. This translates to improved sensitivity to high-mass *HH* resonant searches and a complementary handle on the resolved analyses toward the observation of the SM *HH* process, as well as measurements of certain couplings, including $\kappa_{2V}$. Resolved topologies will continue to play an essential role in the overall *HH* physics program, as the low-$m_{HH}$ events that are characteristic of BSM values of $\kappa_\lambda$ are characterized by low-momenta decay products from the Higgs bosons and thus are much more spherical events. Regardless of whether a boosted or resolved topology is targeted, the efficient and precise identification of physics objects is essential, as is the correct association of these objects to the corresponding Higgs boson to precisely reconstruct *HH*.

## 3.2. Physics Object Reconstruction and Identification

While the reconstruction and identification of photons, electrons, and muons are highly efficient and the performance of these algorithms has been relatively stable over the past decade, the reconstruction and identification of jets originating from the hadronization of *b* quarks and $\tau$ leptons has improved far beyond what was considered possible even only a few years ago, thanks to the extensive use of AI techniques. Further improvements in $\tau$- and *b*-tagging algorithms are on the horizon for Run 3 and beyond, and these will play a central role in the overall sensitivity of ATLAS and CMS to *HH* processes as a result of the mass-dependent couplings of the Higgs boson.

**3.2.1. Bottom quarks.** The most probable decay mode of the Higgs boson involves its transformation into a pair of *b* quarks, which are the heaviest quarks accessible in Higgs boson decays. Identifying the presence of these *b* quarks is crucial for understanding Higgs boson interactions. Hadrons containing *b* quarks have longer lifetimes ($c\tau \sim 500$ μm) compared with lighter quarks and travel a few millimeters to centimeters through the detector, depending on their momenta. The distance traveled translates to tracks and vertices that are displaced with respect to the primary interaction vertex in the event. The main challenges in *b* jet identification include misidentifying jets initiated by *c* quarks, lighter-flavor quarks, or gluons. Jets initiated by *c* quarks (*c* jets) can be misidentified as *b* jets due to the relatively large mass and long lifetime of *c* hadrons, along with the presence of *c* hadrons in the *b* hadron decay chain. Lighter-flavor quarks or gluons may also be misidentified as *b* hadrons as a result of detector resolution effects during the reconstruction of secondary vertices and impact parameters, arising from interactions of hadrons with the detector, or decays of long-lived particles.

Both the ATLAS and CMS Collaborations have developed dedicated algorithms, incorporating advanced deep learning (DL) techniques, to identify jets originating from the hadronization of *b* quarks—a process known as *b*-tagging. The latest generation of *b*-tagging algorithms utilizes

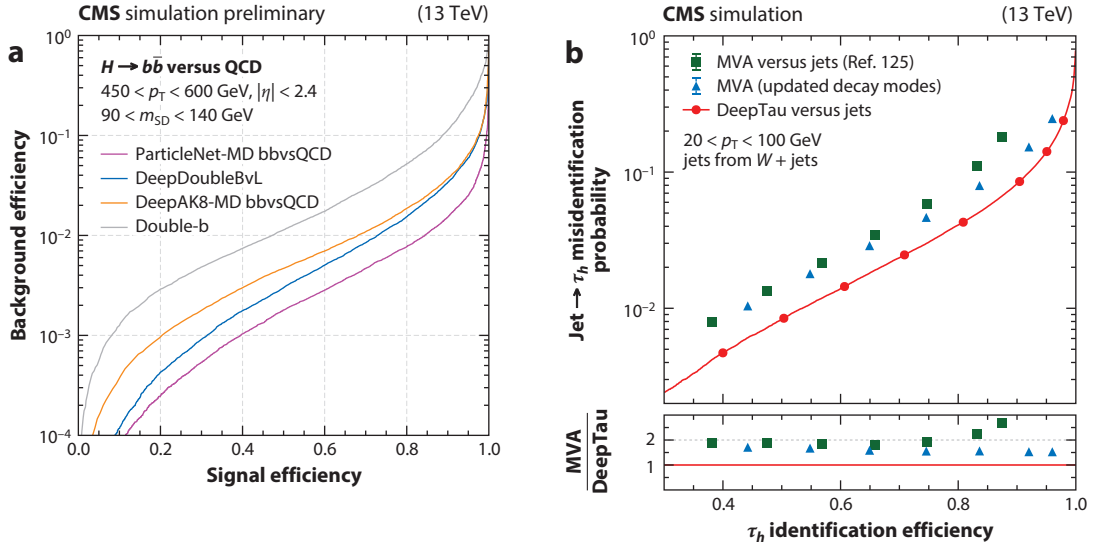


**Figure 3**

(*a*) Performance of different algorithms in identifying a pair of *b* quarks from the Higgs boson decay for large-*R* jets with $450 < p_T < 600$ GeV. The figure shows the efficiency for jets from QCD-initiated multijet production to pass the discriminator versus the efficiency for genuine *b* jets. For details of the design of the different algorithms, see Reference 64. (*b*) Efficiency with which quark- or gluon-initiated jets pass different $\tau$ identification discriminators versus the efficiency for genuine $\tau_h$, for jets with $20 < p_T < 100$ GeV (66). Panel *a* adapted from Reference 64 (CC BY 4.0). Panel *b* adapted from Reference 66 (CC BY 4.0).

lower-level information, such as reconstructed particles and displaced vertices, processed with DL techniques. For small-*R* jets, ATLAS and CMS employ similar approaches, utilizing algorithms based on convolutional and recurrent neural networks (61–63). In large-*R* jet identification, CMS employs more advanced techniques based on graph neural networks (64, 65).

For small-*R* jets, the indicative performance figures are an approximately 70% *b*-tagging efficiency with a background rejection of 25 (1,000) for *c* (lighter-quark or gluon) jets. In the case of large-*R* jets, a 70% efficiency for correctly identifying a pair of *b* quarks results in an inclusive rejection factor of around 250 for background processes. **Figure 3*a*** shows the performance of different algorithms in identifying a pair of *b* quarks from the decay of a Higgs boson, for large-*R* jets. The state-of-the-art algorithm ParticleNet yields an improvement by a factor of two to ten in the rejection of other jet flavors, compared with previous generations of algorithms.

The search for *HH* relies heavily on the ability to reconstruct accurately the masses of the two Higgs boson candidates. Therefore, the collaborations have also focused on enhancing the reconstruction of *b* jets. An accurate estimation of the *b* jet energy is complicated by the fact that jets initiated from *b* quarks contain *b* hadrons that have a relatively high probability (~35%) of decaying to leptons and neutrinos. The presence of undetected neutrinos in these semileptonic decays leads to a lower measurable energy compared with that of lighter quarks or gluon jets. Additionally, because of the soft particles resulting from the decay of heavy hadrons, *b* jets exhibit a broader energy deposition cone than do light jets. To this end, dedicated energy corrections have been developed to improve *b* jet reconstruction.

The ATLAS Collaboration addresses these effects in small-*R* jets by using a rule-based approach that capitalizes on the fact that muons, which constitute around 15% of *b* hadron decays, are not considered in the standard ATLAS jet calibration workflow. In this approach, *b* jets undergo an additional correction if a muon is detected in proximity to the jet. This correction involves

adding the four-momentum of the muon to that of the jet (67). Additional residual jet momentum corrections are applied (67) to better account for escaping neutrinos and ensure a consistent response for jets containing semileptonic and hadronic decays of $b$ hadrons. An improvement in the $H \to b\bar{b}$ invariant mass resolution of approximately 20% has been achieved, relative to the calibration without including muons.

The CMS Collaboration addresses this challenge through the development of a dense neural network (DNN)-based $b$ jet energy regression algorithm (68), featuring inputs for jet structure, information related to reconstructed secondary vertices, and soft leptons from semileptonic decays (when available). A specialized loss function enables the simultaneous training of an energy correction and a per-jet resolution estimator. The DNN regression significantly enhances the $b$ jet resolution by up to ∼15%, which translates to an improvement of ∼20% in $m_{HH}$. The resolution estimator predicted by the DNN, based on quantile estimators, demonstrates the ability to predict the intrinsic jet resolution with an accuracy of better than 20% across a momentum range spanning more than one order of magnitude.

In the context of boosted jets, as described above, grooming techniques are designed to enhance the $H \to b\bar{b}$ mass ($m_{b\bar{b}}$) resolution. However, owing to their simplicity, these algorithms may occasionally either (*a*) remove genuine jet constituents accounting for a significant fraction of the jet momentum, leading to a jet mass considerably smaller than expected, or (*b*) fail to eliminate jet constituents originating from sources other than the hadronization of the $b$ quarks, resulting in increased jet masses. To refine the jet mass estimation, the CMS Collaboration developed a regression algorithm, using the ParticleNet architecture as for $H \to b\bar{b}$ identification, to predict the jet mass (69). This approach improves $H \to b\bar{b}$ reconstruction efficiency by ∼40% and yields an improvement in $m_{b\bar{b}}$ resolution of around a factor of two.

**3.2.2. $\tau$ identification.** The $\tau$ is the heaviest lepton, with a mass of 1.776 GeV and a lifetime of $c\tau \sim 87$ μm. As a result of its substantial mass, the $\tau$ is the only lepton with hadronic decays. In ∼65% of cases, the $\tau$ decays hadronically, typically producing either one or three charged mesons, mainly pions, that are referred to as one- and three-pronged $\tau$ decays, respectively. The decay can also include up to two neutral pions that subsequently decay into a pair of photons. While leptonic $\tau$ decays are reconstructed as prompt electrons or muons, the hadronic decays of a $\tau$ (denoted $\tau_h$) are reconstructed by combining information on the visible decay products, such as track momenta and impact parameters, as well as energy clusters associated with the $\tau$ candidate. $\tau_h$ decays are typically narrower than a quark- or gluon-initiated jet and are characterized in the calorimeter by a collimated, and well-isolated, energy deposit. As for $b$ jet identification, DL techniques have proven to be extremely powerful in improving the identification of $\tau_h$.

In ATLAS, $\tau_h$ detector objects are seeded by small-$R$ jets (70), while in CMS, $\tau_h$ reconstruction is performed using an algorithm that combines information from the energy deposited in the calorimeters and from the reconstructed charged tracks (66). Both experiments have developed DL-based algorithms (66, 71) that use track and calorimeter information to reduce the misidentification rate of quark- or gluon-initiated jets as $\tau_h$ objects. **Figure 3*b*** shows the efficiency at which quark- and gluon-initiated jets pass different $\tau$ identification discriminators used in CMS versus the efficiency for genuine $\tau_h$. The developments yield an approximately twofold-improved background rejection factor compared with the previous state-of-the-art tools for the same $\tau_h$ efficiency. Both CMS and ATLAS have achieved similar performance. For example, the "loose" working point used in the ATLAS $HH \to b\bar{b}\tau^+\tau^-$ analyses provides a background rejection factor of 21 (90) for an 85% (75%) efficiency of selecting true one-prong (three-prong) $\tau$s (71).

Analogous to boosted $H \to b\bar{b}$ scenarios, dedicated algorithms have been developed to identify boosted $H \to \tau^+\tau^-$ decays occurring within a single large-$R$ jet. The ATLAS and CMS

experiments have developed similar strategies for identifying boosted $\tau\tau$ objects (72, 73) and have used them to search for high-mass resonances decaying to Higgs bosons in a $b\bar{b}\tau^+\tau^-$ final state. The algorithms start by identifying the presence of two energy clusters within the large-$R$ jet using the approach described in References 72 and 73. The tools developed for single-$\tau$ reconstruction are adapted to reconstruct individual $\tau$s within these clusters. The reconstructed $\tau$s are then processed simultaneously using multivariate techniques to improve their discrimination against quark- or gluon-initiated jets, electrons, and muons. The identification efficiency for $H \to \tau^+\tau^-$ is ∼60% for a misidentification rate of $\sim 10^{-4}$ against typical backgrounds.

## 4. EXPERIMENTAL STATUS OF SEARCHES FOR HIGGS BOSON PAIRS

As we transition away from the foundational aspects of experimental techniques and tools essential for $HH$ searches, we discuss in this section the current experimental status of the pivotal search channels at the LHC. We systematically dissect the progress made in various analysis channels, scrutinizing both the results achieved and the challenges that persist. This section aims to provide a comprehensive overview of the experimental efforts, highlighting key findings, ongoing efforts, and the potential impact of these searches on our understanding of particle physics.

### 4.1. $HH \to b\bar{b}b\bar{b}$

The $HH \to b\bar{b}b\bar{b}$ decay mode has the largest branching ratio (34%). Pursuing these $H \to b\bar{b}$ decays, however, presents challenges, as multijet processes including jets initiated by heavy-flavor quarks have cross sections that are several of orders magnitude higher than the $HH$ signal cross section and, consequently, present a formidable background to this search channel.

Traditionally, the exploration of the nonresonant $HH \to b\bar{b}b\bar{b}$ channel by both ATLAS (74, 75) and CMS (76) has concentrated on moderately Lorentz-boosted Higgs bosons, with the aim of resolving all four $b$ quarks into distinct small-$R$ jets. The CMS Collaboration also introduced an analysis exploiting the boosted topology (77), which targets Higgs bosons with a larger Lorentz boost. The former approach provides greater signal acceptance, particularly for the triangle diagram that dominates in the low-$m_{HH}$ region. However, it comes with higher contributions from multijet background processes and greater ambiguity in the pairing of $b$ jets into Higgs boson candidates. The lower signal acceptance of the boosted analysis event selection is compensated for with higher signal purity and improved background suppression via the exploitation of correlations between $b$ quarks in the same large-$R$ jet. A statistical combination of both CMS analyses was performed to maximize the overall sensitivity of the $HH \to b\bar{b}b\bar{b}$ channel.

In the resolved topology, effective $b$-tagging techniques, as described in Section 3.2.1, play a crucial role in identifying the four most likely small-$R$ jets originating from the decay of the Higgs bosons. The ATLAS (74) and CMS (76) analyses enhance discrimination between the $HH \to b\bar{b}b\bar{b}$ signal and SM backgrounds by constructing an event-level discriminant using boosted decision trees (BDTs). The BDT inputs encompass kinematic information, correlations between the $b$ jets, and other objects within the event, along with more comprehensive event-level data. Another discriminant has been developed to differentiate signals produced in $gg$F or VBF production. The primary background in the resolved topology arises from multijet production. It is imperative to note that, in recognition of the unreliability of simulations for estimating multijet production, both the ATLAS and CMS analyses employ a similar data-driven approach for the estimation of this background, namely specific data control regions, designed to be distinct from the signal region but with similar characteristics. These regions involve criteria based on the number of identified $b$ jets and selections on $m_H$. With the aid of sophisticated AI techniques, these data

control regions are used to infer the shape of the event-level discriminant and account for any differences in the normalization of the multijet process between the data and simulation in the signal region.

In the boosted topology explored by CMS, an additional power in sensitivity has been achieved. Despite the smaller signal acceptance, the application of advanced DL-based algorithms for jet identification, as discussed in Section 3.2.1, has played a pivotal role in enhancing this sensitivity, and the multijet background is suppressed to such an extent that the contribution from the $t\bar{t}$ process also becomes important. CMS has developed a data-driven strategy to address the challenges in estimating these backgrounds, particularly the QCD multijet one. This strategy exploits the fact that, by design, the response of the $H \to b\bar{b}$ tagging algorithm is independent of the mass of the large-$R$ jet, enabling a reliable estimation with minimal systematic uncertainties.

These analyses are used to establish upper limits on the $HH$ production cross section at a 95% confidence level (CL), based on the CL$_s$ criterion and derived using asymptotic formulas (78–81). For the ATLAS analysis, the observed (expected) limit on the total $HH$ production cross section relative to the SM prediction is 5.4 (8.1); for the CMS analysis, the corresponding value is 6.4 (4.0). The resolved CMS analysis yields a sensitivity comparable to that of the ATLAS analysis, with an observed (expected) upper limit of 3.9 (7.8). The results of the analysis are interpreted in the context of the $\kappa$ framework (82, 83). ATLAS has set an observed (expected) 95% CL interval of $\kappa_\lambda \in [-3.9, 11.1]$ ($[-4.6, 10.8]$), and CMS has set $\in [-2.2, 9.9]$ ($[-4.0, 9.2]$) for a combination of the resolved and boosted channel results. These intervals assume that all other Higgs boson couplings are at their SM values. In the CMS analysis, especially for lower $\kappa_\lambda$ values resulting in softer decay products and $m_{HH}$ spectrum, the sensitivity is driven by the resolved topology. A noteworthy advancement is made in the boosted analysis (77), representing a significant step in understanding the four-point interaction of two $V$ bosons and two Higgs bosons, accessible in the VBF production mode. The absence of a sizable observable VBF $HH$ signal has, for the first time, established a nonzero value of $\kappa_{2V}$ with a significance of $6.3\sigma$, assuming that other Higgs boson couplings are fixed to their SM values.

## 4.2. $HH \to b\bar{b}\tau^+\tau^-$

The $HH \to b\bar{b}\tau^+\tau^-$ final state provides one of the largest branching fractions, approximately 7%, with smaller contributions from SM background processes compared with the $HH \to b\bar{b}b\bar{b}$ channel, while allowing for efficient $\tau$ identification. As a result, this channel has emerged as a powerful probe of nonresonant $HH$ production.

The cornerstone of this analysis is the efficient reconstruction of the $H \to \tau^+\tau^-$ and $H \to b\bar{b}$ systems. Both ATLAS (84) and CMS (85) consider final states with either two $\tau_h$s or one $\tau_h$ and the other decaying to leptons. These decay modes constitute almost 90% of the total di-$\tau$ decay branching ratio. The distinct final states are designed to be statistically independent and are combined for the final result. The misidentification of $\tau_h$ is suppressed using the DL-based algorithms described in Section 3.2.2.

In the case of $H \to b\bar{b}$, ATLAS targets the resolved regime, where each $b$ jet is reconstructed as a distinct small-$R$ jet, whereas CMS exploits both resolved and boosted topologies. The identification techniques discussed in Section 3.2.1 are employed to identify the $b$ and $b\bar{b}$ jets. CMS has developed a new DNN-based algorithm to resolve ambiguities in $b$ jet and $\tau_h$ identification and construct the $H \to b\bar{b}$ candidate. The input features of this network include information about the $b$ jets, the $H \to \tau^+\tau^-$ system kinematic variables, and correlations between the physics objects. For each event, all possible $b$ jet candidates are assigned a score by the $HH$-tag algorithm; the two jets with the highest scores are taken as those originating from the decay of the Higgs boson. This

development has resulted in a 10% relative improvement in the purity of the $H \to b\bar{b}$ candidate, reaching 95%. ATLAS deemed an equivalent algorithm unnecessary.

An additional challenge in this analysis arises from the undetected energy from the neutrinos produced in $\tau$ decays, which leads to an underconstrained kinematic description of the system. To address this challenge, both collaborations have developed algorithms to account for the invisible part of the four-momentum of the di-$\tau$ system due to the neutrinos. ATLAS uses the Missing Mass Calculator (MMC) algorithm (86), whereas CMS uses the Secondary Vertex Fit (SVfit) algorithm (87). Both algorithms calculate the best estimate of the $H \to \tau^+\tau^-$ mass ($m_{\tau^+\tau^-}$) on an event-by-event basis, using constraints from the measurements of the visible decay products and the missing transverse momentum ($p_{\mathrm{T}}^{\mathrm{miss}}$). The MMC estimate exploits the fact that the solutions of the underconstrained kinematic system are not all equally probable. Then, additional constraints from the $\tau$ kinematics are applied. In this case, the distance $\Delta R$ between the neutrino(s) and the visible decay products is parameterized and provides a probability density function that is then incorporated in a global event likelihood. The most probable value provides the final estimation of $m_{\tau^+\tau^-}$. Similarly, the SVfit $m_{\tau^+\tau^-}$ values are reconstructed by exploiting a set of the observables similar to the ATLAS ones. The model predicts the probability of observing the $p_{\mathrm{T}}^{\mathrm{miss}}$ values measured in the event, given a parameterization of the kinematics of the $\tau$ pair decay, and provides a probability density function as a function of the unknown parameters. The best estimate for $m_{\tau^+\tau^-}$ is the value that maximizes this probability. Neutrinos from semileptonic decays of $B$ hadrons also contribute to the overall $p_{\mathrm{T}}^{\mathrm{miss}}$ of signal events, and the $m_{b\bar{b}}$ reconstruction is improved by applying dedicated $b$ jet–specific energy corrections, as discussed in the preceding section. To suppress the backgrounds that are discussed further below, CMS selects events with $m_{\tau^+\tau^-}$ and $m_{b\bar{b}}$ values around $m_H$, while ATLAS removes events with low $m_{\tau^+\tau^-}$.

The main backgrounds to the $HH \to b\bar{b}\tau^+\tau^-$ process are $Z \to \tau^+\tau^-$ produced in association with heavy-flavor jets, $t$ quark pair ($t\bar{t}$) production, and multijet processes in which quark- and gluon-initiated jets are misidentified as $\tau_h$. Single-Higgs production, particularly in association with a $Z$ boson or $t\bar{t}$, is becoming an important background contribution as the size of the available data set increases. Both ATLAS and CMS estimate the main backgrounds listed above by using a combination of simulation and dedicated control regions in the data.

To further suppress the backgrounds, ATLAS and CMS exploit multivariate techniques—BDTs and neural networks for ATLAS and DNNs for CMS—to enhance the discrimination between signal and background processes. The physics object properties and their correlations, and observables related to the event properties like the $m_{HH}$, are used to separate the signal from the backgrounds. Both collaborations have derived upper limits on the $HH \to b\bar{b}\tau^+\tau^-$ cross section; the observed (expected) upper limit is 4.7 (3.9) and 3.3 (5.2) for ATLAS and CMS, respectively, assuming $\kappa_\lambda = 1$. The dominant source of systematic uncertainty, contributing around 80% of the total systematic uncertainty, is due to the limited quantity of data in the control regions used to estimate the main backgrounds. In both experiments, around 70% of the sensitivity comes from the hadronic final state. The boosted topology used in CMS is relevant primarily for constraining modifications to $\kappa_{2V}$. The results are interpreted in the $\kappa$ framework and yield observed (expected) constraints of $-3.2 < \kappa_\lambda < 9.1$ ($-2.5 < \kappa_\lambda < 9.2$) in the case of ATLAS and $-1.7 < \kappa_\lambda < 8.7$ ($-2.9 < \kappa_\lambda < 9.8$) for CMS. The difference in expected limits on the cross section and, to a much lesser extent, $\kappa_\lambda$ has not been fully explored, but it is noteworthy that the two experiments report substantial differences in their efficiencies for triggering on events in the most sensitive fully hadronic channel. The efficiency for SM $HH$ events that pass a loose set of offline reconstruction requirements on the $\tau$s and $b$ jets to also pass the trigger is 69% for ATLAS (88) and 34% for CMS (89).

### 4.3. $HH \to b\bar{b}\gamma\gamma$

An additional channel involves the exploration of nonresonant $HH$ production via $gg$F and VBF in final states featuring two photons and two $b$ quarks. Despite its very small branching fraction of approximately 0.3%, this final state presents a distinct and clean signature thanks to the decay of one of the Higgs bosons to two isolated photons. Excellent photon energy resolution allows the $H \to \gamma\gamma$ decay to be reconstructed precisely, and low backgrounds allow for a far less restrictive online selection that makes accessible the events populating the lower $m_{HH}$ region, where the contribution from the triangle diagram (**Figure 2*b***) dominates. Another advantage of the $HH \to b\bar{b}\gamma\gamma$ channel is that there is no combinatorial background in resolving the two Higgs bosons. The techniques discussed in Section 3.2.1 are used to reconstruct the $H \to b\bar{b}$ candidate.

The main background comprises nonresonant $b\bar{b}\gamma\gamma$ production, followed by single-Higgs production in association with $t\bar{t}$ ($t\bar{t}H$). The ATLAS (90) and CMS (91) analyses have developed AI techniques to further suppress the main backgrounds. The CMS analysis (91) employed one discriminant designed to suppress the nonresonant diphoton background ($t\bar{t}\gamma\gamma$, $\gamma\gamma$+jets, and $\gamma$+jets), using event and object kinematic variables, object identification variables, and object resolution variables as inputs. CMS developed a second discriminant to reduce the $t\bar{t}H$ background. This discriminant uses a combination of lower-level information from the individual reconstructed particles and higher-level features describing kinematic properties of the event, including angular variables between physics objects, information useful to identify leptonic decays of $W$ bosons produced in the $t$ quark decay, and variables to distinguish hadronic decays of $W$ bosons. CMS then uses the output of the discriminants to define mutually exclusive analysis categories. The $HH \to b\bar{b}\gamma\gamma$ signal is extracted from a two-dimensional fit to the invariant masses of the $H \to b\bar{b}$ and $H \to \gamma\gamma$ candidates simultaneously in all categories.

The ATLAS analysis (90) uses a single BDT trained separately in low-mass ($m_{HH} < 350$ GeV) and high-mass ($m_{HH} > 350$ GeV) regions to separate the $gg$F and VBF $HH$ signal from diphoton and single-Higgs background processes. Similarly to the CMS analysis, ATLAS uses the output BDT score to define orthogonal signal regions and the signal extracted from a one-dimensional fit to the diphoton mass distribution.

The observed (expected) upper limit at 95% CL on the $HH$ production cross section in the ATLAS (90) and CMS (91) analyses is 4.0 (6.4) and 7.7 (5.2) times the SM prediction, respectively. The observed (expected) 95% CL interval for $\kappa_\lambda$ is $[-1.4, 6.9]$ ($[-2.8, 7.8]$) in the case of ATLAS; CMS obtains a similar sensitivity, yielding $\kappa_\lambda \in [-3.3, 8.5]$ ($[-2.5, 8.2]$). These intervals assume that all other Higgs boson couplings are at their SM values. The improvements introduced in the analysis techniques by both experiments yield an increase in sensitivity by approximately a factor of two, compared with the previous incarnation of the analyses, in addition to the one expected by the additional data analyzed.

### 4.4. Summary of Higgs Boson Pair Production Measurements in LHC Run 2

The three channels discussed above, namely $HH \to b\bar{b}b\bar{b}$, $HH \to b\bar{b}\gamma\gamma$, and $HH \to b\bar{b}\tau^+\tau^-$, provide the largest sensitivity on $\lambda_{HHH}$. Nevertheless, the collaborations have explored several other decay modes that, with the current data set, yield significantly weaker sensitivity. However, there is still potential to be unlocked in some of these other channels. For instance, decay modes such as $HH \to \gamma\gamma VV^*$ offer a clean diphoton signature and may contribute more to final combinations as more data are collected and the channel becomes less statistically limited. Alternatively, more complex decay modes like $HH \to b\bar{b}VV^*$ are expected to exhibit significant improvements by incorporating more sophisticated physics object reconstruction algorithms and analysis strategies.

**Table 1 Constraints on the *HH* cross section as multiples of the Standard Model prediction, and on $\kappa_\lambda$, all at 95% confidence level[a]**

| Experiment/channel | | Reference(s) | $\sigma_{HH}$ | | $\kappa_\lambda$ | |
|---|---|---|---|---|---|---|
| | | | Expected | Observed | Expected | Observed |
| ATLAS | $HH \to b\bar{b}\gamma\gamma$ | 102[b] | 5.0 | 6.4 | [−2.8, 7.8] | [−1.4, 6.9] |
| CMS | | 91 | 5.2 | 7.7 | [−2.5, 8.2] | [−3.3, 8.5] |
| ATLAS | $HH \to b\bar{b}\tau^+\tau^-$ | 84 | 3.9 | 4.7 | [−2.0, 9.0] | [−2.4, 9.2] |
| CMS | | 85 | 5.2 | 3.3 | [−1.8, 8.7] | [0.7, 6.4] |
| ATLAS | $HH \to b\bar{b}b\bar{b}$ (resolved) | 74 | 8.1 | 5.4 | [−4.6, 10.8] | [−3.9, 11.1] |
| CMS | | 76 | 7.8 | 3.9 | [−5.0, 12.0] | [−2.3, 9.4] |
| CMS | $HH \to b\bar{b}b\bar{b}$ (boosted) | 77 | 5.1 | 9.9 | [−5.1, 12.2] | [−9.9, 16.9] |
| ATLAS | $HH \to b\bar{b}\ell\ell + E_{\mathrm{T}}^{\mathrm{miss}}$ | 100[b] | 16.2 | 9.7 | [−8.1, 15.5] | [−6.2, 13.3] |
| CMS | $HH \to 4W, 2W2\tau, 4\tau$ | 96 | 19.4 | 21.3 | [−6.9, 11.7] | [−6.9, 11.1] |
| CMS | $HH \to ZZ^*b\bar{b} \to 4\ell b\bar{b}$ | 98 | 39.6 | 32.4 | [−9.8, 15.0] | [−8.8, 13.4] |
| ATLAS | Combination | 99[b] | 2.9 | 2.4 | [−1.9, 7.6] | [−0.4, 6.3] |
| CMS | | 103[b] | 2.5 | 3.4 | [−2.0, 7.7] | [−1.2, 7.5] |

[a]All results use the full Run 2 data set ($\sqrt{s} = 13$ TeV, ∼140 fb$^{-1}$).

[b]Constraints on $\kappa_\lambda$ for these results are determined from a likelihood scan and are quoted at $2\sigma$ confidence. The constraints derived from likelihood scans assume the presence of an *HH* signal, whereas the 95% exclusion limits assume an absence of signal, and for this reason, the results obtained with the different methods cannot be directly compared.

A detailed discussion of the analysis of these decay modes extends beyond the scope of this review but is available elsewhere (92–98).

**Table 1** summarizes our current understanding of the Higgs self-interaction. Both ATLAS and CMS have designed their analyses to enable statistical combination, and the last row of the table presents the statistical combination of the channels. The statistical combination of ATLAS results (99) does not include the $HH \to b\bar{b}\ell\ell + E_{\mathrm{T}}^{\mathrm{miss}}$ channel result (100) and uses an older version of the $HH \to b\bar{b}\gamma\gamma$ analysis (101) than the newer result quoted in the table.

## 4.5. Constraints from Single-Higgs Measurements and *HH* + *H* Combination

Building on the discussion in Section 2.3, single-Higgs processes are essential not only for providing a different perspective on measuring $\lambda_{HHH}$ but also for understanding how other Higgs boson couplings can affect *HH* cross sections. Specifically, the *gg*F *HH* cross section depends primarily on the Higgs boson coupling to the *t* quark, while the VBF *HH* depends on the Higgs boson couplings to *V* bosons. Additional dependencies on Higgs boson couplings can emerge when different *HH* decay channels are considered. However, the current ATLAS and CMS data set is insufficient to simultaneously constrain $\kappa_\lambda$ and the Higgs boson couplings to fermions and *V* bosons from *HH* cross sections. This limitation arises because deviations in different Higgs boson couplings can have indistinguishable effects on *HH* cross sections within the experimental precision achievable with the available data. To address this issue, both experiments designed the *H* and *HH* analyses with minimal statistical overlap, allowing the development of a framework for a global fit to simultaneously constrain the Higgs self-coupling and other coupling modifiers. The model-dependent assumptions of this parameterization are described elsewhere (99). **Figure 4** presents the observed and expected constraints in the $\kappa_\lambda$–$\kappa_t$ plane from single-Higgs and double-Higgs analyses, as well as their combination.

The inclusion of single-Higgs measurements enhances the constraints on $\kappa_\lambda$ compared with previous *HH* searches, where other Higgs boson couplings were typically assumed to be equal to

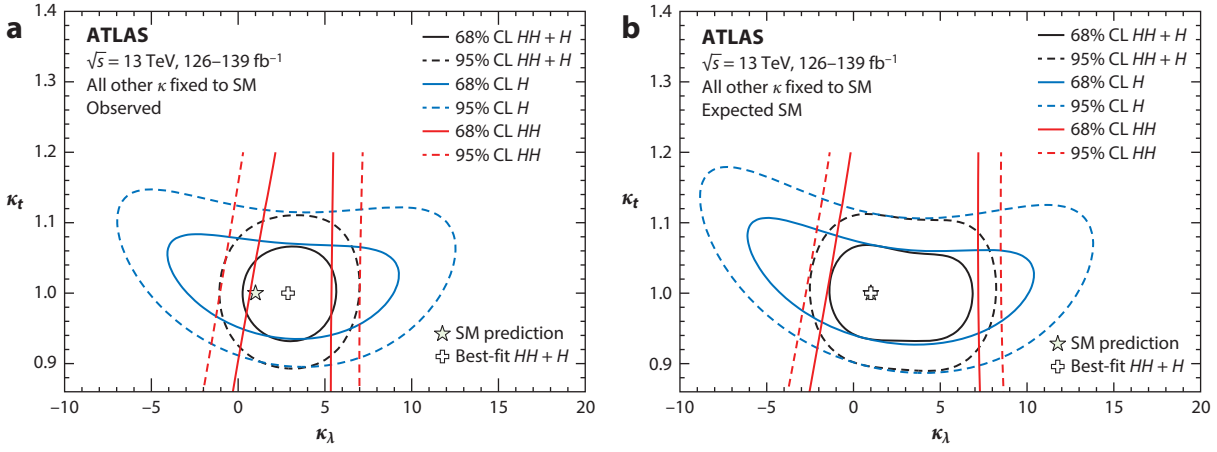


**Figure 4**

(*a*) Observed and (*b*) expected constraints in the $\kappa_\lambda$–$\kappa_t$ plane from single-Higgs (*blue*) and double-Higgs (*red*) analyses and their combination (*black*) using the ATLAS analysis (99). The solid (dashed) lines represent the 68% (95%) confidence level (CL) contours. The double-Higgs contours are shown for $\kappa_t$ values lower than 1.2. The observed constraint for the single- and double-Higgs combination for $\kappa_t$ values below unity is slightly less stringent than that for the single-Higgs fit alone due to the slightly higher best-fit value for this coupling modifier. Figure adapted from Reference 99 (CC BY 4.0).

their SM values. This combination also allows for more generic interpretations, where constraints on $\kappa_\lambda$ and other Higgs boson couplings are obtained simultaneously from the data. In the combined single-Higgs and double-Higgs analyses, an observed (expected) exclusion of $-1.4 < \kappa_\lambda < 6.1$ ($-2.2 < \kappa_\lambda < 7.7$) is achieved at 95% CL in this less model-dependent fit. The values of all other coupling modifiers agree with the SM prediction within uncertainties.

## 4.6. Resonant Higgs Boson Pair Production

This article focuses primarily on the search for SM *HH* production. However, searches for BSM models that predict interactions of heavy resonances directly coupling to a pair of Higgs bosons represent an important element of the LHC physics program. Such scenarios introduce an additional source of *HH* production in resonant topologies, a feature absent from the SM. Given the relatively small cross section of SM *HH* production, which is dictated by destructive interference of the LO diagrams, final states with resonant production of two Higgs bosons could serve as prominent indicators of the existence of BSM heavy resonances.

Several extensions of the SM could give rise to resonant production of Higgs bosons. Models with extended Higgs sectors, encompassing more than the single complex Higgs doublet of the SM, provide natural candidates for heavy Higgs bosons that decay into final states involving one or more Higgs bosons. Examples of such models include two-Higgs-doublet models (2HDMs) (104), models with two Higgs doublets extended with a scalar singlet (105), and the two-real-singlet model (106). Supersymmetry is another framework that naturally incorporates extended Higgs sectors, such as the minimal supersymmetric model featuring a 2HDM-type Higgs sector and the next-to-minimal supersymmetric model (107–109), among many other possibilities.

Once produced, Higgs bosons can decay in various ways, each leading to a distinct final state. As mentioned above, the most common Higgs decay mode is into a pair of $b$ quarks, followed by decays into pairs of $W$ bosons and $\tau$ leptons. Methodologies similar to those discussed above for physics object reconstruction and identification in the case of nonresonant *HH* production, as well as analysis techniques, have been explored in this context. Since a comprehensive discussion of the

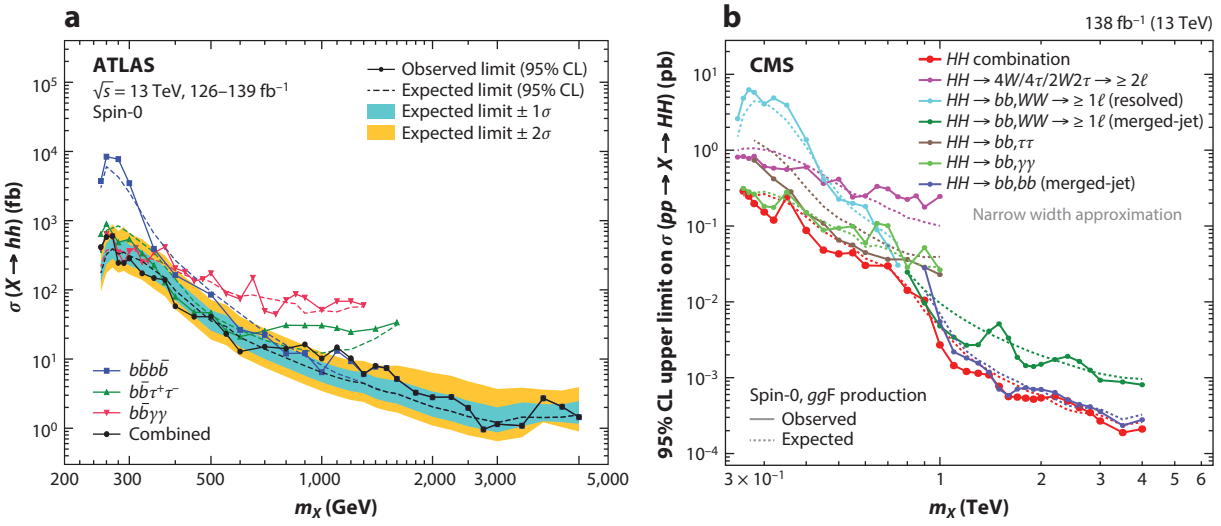


**Figure 5**

Observed and expected 95% confidence level (CL) upper limits on the cross section for a new particle, $X$, decaying to a pair of SM Higgs bosons with a mass of 125 GeV, $h$, as a function of the resonance mass, $m_X$, from (*a*) ATLAS and (*b*) CMS. Panel *a* adapted from Reference 110 (CC BY 4.0). Panel *b* adapted from Reference 111 (CC BY 4.0).

numerous analyses exploring these BSM models goes beyond the scope of this article, we present only a summary of the current status. **Figure 5** shows the combination of resonant $HH$ searches from the ATLAS (110) and CMS (111) experiments.

## 5. CHALLENGES, PROSPECTS, AND FUTURE DIRECTIONS OF THE FIELD

Measuring the Higgs self-coupling to a high precision will be one of the highest priorities for experiments at future colliders (112). Projections for the precision with which we can measure $\kappa_\lambda$ at the HL-LHC have improved rapidly over the past few years. Less than a decade ago, it was still widely believed that meaningful measurements of the Higgs self-coupling would be out of reach at the HL-LHC. By 2018, the outlook had improved almost beyond recognition, and a combination of ATLAS and CMS projections (113) predicted that a precision of 50% on $\kappa_\lambda$ would be achievable with 3,000 fb$^{-1}$ of data. This improvement over earlier expectations was driven largely by the widespread adoption of AI techniques throughout the full analysis chain. These improvements have made the hadronic channels $HH \rightarrow b\bar{b}b\bar{b}$ and $HH \rightarrow b\bar{b}\tau^+\tau^-$ not only viable but also the most sensitive search channels for $\kappa_{2V}$ and cross-section measurements. In the following subsections, we review the experimental challenges that lie ahead in the quest to understand the Higgs boson's self-interaction and describe the prospects for measuring it in the future.

Caution when considering sensitivity projections is warranted. Although physics processes and detector response can be simulated, we can predict neither future technologies nor the creativity of the analyses that will determine what will ultimately be achieved. For example, note that 2015 estimates made by the ATLAS Collaboration of the sensitivity of the $HH \rightarrow b\bar{b}\tau^+\tau^-$ process with 3,000 fb$^{-1}$ of data (114) were surpassed a short time later with the use of a data set one-twentieth the size (84).

## 5.1. Experimental Challenges

To reach the potential of observing Higgs boson pair production at the (HL-)LHC requires several experimental challenges to be addressed. The most important ones stem from the need both to explore the low-$m_{HH}$ regime, which is overwhelmed by background processes, and to enhance the role of boosted topologies in $HH$ production searches and measurements.

**5.1.1. Importance of the low-$m_{HH}$ regime in $\kappa_\lambda$ measurements.** The $m_{HH}$ shape changes as the strength of the Higgs self-coupling relative to the SM prediction is varied, as a result of interference between the top box (**Figure 2*a***) and triangle (**Figure 2*b***) diagrams. Measuring the shape of the $m_{HH}$ distribution is therefore a crucial ingredient in measuring the self-coupling strength, and the most valuable information is concentrated in the lowest-$m_{HH}$ regions.

The power of the low-$m_{HH}$ region in constraining the self-coupling is demonstrated in analyses of the $HH \to b\bar{b}\gamma\gamma$ channel. The inclusion of a dedicated signal region targeting events with $m_{HH} < 350$ GeV, in an updated projection of the sensitivity of the ATLAS $HH \to b\bar{b}\gamma\gamma$ analysis at the HL-LHC (115), improves the $1\sigma$ ($2\sigma$) CL upper limit of $\kappa_\lambda$ to 1.9 (4.6), compared with 2.5 (8.2) in a previous analysis (113). These low-$m_{HH}$ events are comparatively easy to access in the $HH \to b\bar{b}\gamma\gamma$ channel, but unfortunately that is not the case for the $b\bar{b}\tau^+\tau^-$ and $b\bar{b}b\bar{b}$ channels, where the difficulties of triggering on fully hadronic final states and the challenges of predicting large backgrounds imply that high momentum requirements must be imposed on the decay products. These hadronic channels have been proven to have excellent sensitivity to $HH$ for cross-section measurements that are far less reliant on the low-mass region. Opening up a new low-$m_{HH}$ region of phase space for these channels offers huge potential for improving our knowledge of the Higgs self-coupling that can be extracted from the HL-LHC data set. Accessing this crucial low-$m_{HH}$ portion of the $HH$ phase space will be even more challenging in the high-pileup environments at the HL-LHC, and without innovative new trigger strategies in place to select these events, they risk being lost forever.

**5.1.2. Role of boosted topologies in Higgs boson pair production searches and measurements.** The role of boosted topologies in $HH$ production searches becomes even more pivotal when considering the increased integrated luminosity expected with LHC Run 3 and subsequent runs. While it is true that the signal acceptance for boosted topologies drops at higher momenta, the larger data sets provided by the expected increases in luminosity can compensate for this limitation. With more data, rare events with high-momentum $HH$ become observable, enhancing the potential for detecting and studying these topologies. This increase in integrated luminosity is particularly beneficial for new physics scenarios where $HH$ might be produced from the decay of heavier new particles, a likelihood not as pronounced in the SM processes.

In the case of new physics scenarios involving two Higgs bosons, boosted topologies are especially relevant. This significance arises because new physics processes, such as those involving high-mass resonances decaying into $HH$ naturally lead to highly boosted Higgs bosons. The ability to explore these high-momentum regimes will be crucial for uncovering potential new particles or interactions that could manifest at high energy scales, beyond the reach of current SM predictions.

On the other hand, in SM $HH$ production, the dynamics are somewhat different. The triangle diagram, a key feature in SM $HH$ production, tends to populate lower masses of the $HH$ system. While this means that the $HH$ are less boosted in comparison to some new physics scenarios, the advantage here lies in the signal purity. Boosted topologies are less contaminated by background processes, allowing for a clearer observation of the SM processes. This distinction underscores the

importance of studying both high- and low-momentum regimes to comprehensively understand *HH* production and its implications for both SM and BSM physics.

## 5.2. Prospects for Future Analyses

The future of *HH* research holds significant promise, driven by the increasing luminosity at the (HL-)LHC. Potential developments on both the experimental and theoretical fronts are expected to play a crucial role in advancing our understanding and achieving our research goals.

**5.2.1. Run 3.** Data taking for LHC Run 3 commenced in 2022 and is expected to continue through 2025. During the first 2 years (2022–2023), 70 $\text{fb}^{-1}$ of $pp$ collision data with $\sqrt{s} = 13.6$ TeV were delivered to both ATLAS and CMS. For several reasons, including a helium leak in one of the inner triplets, caused by an electrical surge as a result of falling power lines during a storm in July 2023, and an overall reduction in running time due to the ongoing energy crisis, the data set collected so far is substantially smaller than the ∼120 $\text{fb}^{-1}$ originally expected to have been delivered by this point. The LHC hopes to deliver 90 $\text{fb}^{-1}$ of data per year to each experiment in 2024 and 2025, providing ATLAS and CMS each with a total Run 3 data set of ∼270 $\text{fb}^{-1}$.

Using the Run 2 data sets, ATLAS and CMS respectively have obtained expected upper limits on the *HH* signal strength of 2.9 (99) and 2.5 (103) times the SM prediction. From a naïve extrapolation of the published Run 2 combination results to the sensitivity expected with the combined Run 2 and Run 3 data sets (assuming a scaling equal to the inverse square root of the ratio of integrated luminosities), and under the assumption of a combination of the ATLAS and CMS results, limits on the signal strength will start to approach the SM value.

The full Run 2 results represent a factor of 1.8 (2.6) improvement compared with the ATLAS (30) [CMS (116)] partial Run 2 data set results over the gain expected from the larger data set. These improvements are mostly due to the extensive use of AI at several stages of the analysis workflow, particularly in identifying $\tau_h$s and $b$ jets and in separating the *HH* signal process from backgrounds, as well as in better understanding the physics processes and more targeted analyses. If similar levels of improvement are achieved in the Run 3 analyses [e.g., from the new trigger strategies for hadronic channels implemented by both experiments for Run 3 data taking (88, 89)], then evidence for *HH* production could be obtained with the Run 2 and Run 3 data sets. Assuming the SM holds true, it should already be possible to exclude the $\kappa_\lambda = 0$ hypothesis (i.e., no Higgs self-coupling) simply by combining the ATLAS and CMS Run 2 results. This statement will be made with higher confidence by incorporating the Run 3 data analysis results as well.

Note that the full, published Run 2 combinations do not include recent results from single-channel analyses (100, 102) that would reasonably be expected to improve the final Run 2 limits and extrapolated Run 3 sensitivity. Moreover, the increased $\sqrt{s}$ in Run 3 compared with Run 2 (13.6 TeV versus 13 TeV) increases the *HH* cross section from 31.05 fb to 34.43 fb, a larger relative increase than most background processes, which can also contribute to an improvement in results over what can be expected with a simple luminosity scaling.

**5.2.2. HL-LHC.** With its increased luminosity and upgraded detectors, the HL-LHC offers a unique opportunity to probe the Higgs self-coupling, and projections of the precision with which $\kappa_\lambda$ can be measured at the HL-LHC have improved rapidly over the past few years. Less than a decade ago, it was still widely believed that meaningful measurements of the Higgs self-coupling would be out of reach at the HL-LHC, but by 2018, the outlook had improved almost beyond recognition, and a combination of ATLAS and CMS projections (113) predicted that 50% precision on $\kappa_\lambda$ would be achievable with 3,000 $\text{fb}^{-1}$ of data.

**Table 2 Expected discovery significance for *HH* production and available constraints on $\kappa_\lambda$ at 68% CL under the baseline scenario for systematic uncertainties**

| Experiment/channel | | Reference | Discovery significance | $\kappa_\lambda$ (68% CL) |
|---|---|---|---|---|
| ATLAS+CMS | $HH \to b\bar{b}\gamma\gamma, b\bar{b}\tau^+\tau^-, b\bar{b}b\bar{b}, b\bar{b}ZZ^*(4\ell), b\bar{b}VV^*(2\ell)$ | 113 | $4.0\sigma$ | [0.57, 1.5] |
| ATLAS | $HH \to b\bar{b}\gamma\gamma$ | 115 | $2.2\sigma$ | [0.3,1.9] |
| CMS | | 119 | $2.16\sigma$ | — |
| ATLAS | $HH \to b\bar{b}\tau^+\tau^-$ | 120 | $2.8\sigma$ | [0.3,1.9]∪[5.2,6.7] |
| CMS | | 113 | $1.4\sigma$ | — |
| ATLAS | $HH \to b\bar{b}b\bar{b}$ | 118 | $0.99\sigma$ | [−0.5,6.1] |
| CMS | | 113 | $0.95\sigma$ | — |
| CMS | $HH \to WW^*\gamma\gamma, \tau^+\tau^-\gamma\gamma$ | 121 | $0.22\sigma$ | — |
| ATLAS | $HH \to b\bar{b}\gamma\gamma, b\bar{b}\tau^+\tau^-, b\bar{b}b\bar{b}$ | 118 | $3.4\sigma$ | [0.5,1.6] |

Entries in gray indicate older results that have not yet been updated to include the latest knowledge gained from the full Run 2 analyses.

**Table 2** summarizes the updated projections incorporating analysis improvements implemented in the full Run 2 data-set analyses (117, 118). From a simple calculation assuming the same performance from both experiments, a $5\sigma$ observation of *HH* production appears to be within reach, and the expected precision that can be obtained at the HL-LHC can now be reasonably expected to be in the region of 35% when combining results from both experiments.

**5.2.3. Future colliders.** Measuring the Higgs self-coupling with high precision will be one of the main goals of experiments at future colliders (112). The projections in Reference 113, performed in 2018, were used as inputs to the studies employed in the European Strategy process (112). **Figure 6** shows the expected precision of self-coupling measurements at different future colliders. All estimates of the results achievable at future experiments assume a combination with the expected HL-LHC projection results from 2018. Once the recent projections from the HL-LHC are considered, it seems unlikely that precision measurements of single-Higgs processes made at FCC-*ee* will be able to improve the precision of measurements of $\kappa_\lambda$ in a global fit. This does not detract from the physics case of FCC-*ee*, as precision Higgs measurements will be invaluable for a better understanding of EW symmetry breaking and other indirect constraints on new physics.

To date, studies of the potential of future colliders to measure $\kappa_\lambda$ have focused only on the scenario where the Higgs potential is the one predicted by the SM. Ensuring that the colliders and any associated detectors can also be sensitive to $\kappa_\lambda$ in the eventuality that this scenario deviates from the SM prediction should be an important consideration in the design of future experiments.

Muon colliders offer exciting possibilities to measure the Higgs self-coupling in a clean, low-background environment. The data obtained from muon colliders would also provide information complementary to hadron collider experiments. Such data can help cross-validate and enhance our understanding of the Higgs self-coupling and potentially reveal deviations from the SM.

## 5.3. Triple-Higgs Production and the Quartic Coupling

Accessing the quartic term, $(1/4)\lambda h^4$, is necessary in order to fully determine the shape of the Higgs potential. The cross section for *HHH* production is around three orders of magnitude smaller than that for *HH* production (123), making this process inaccessible at the HL-LHC and extremely challenging to access even in the most aggressive future collider scenarios. Constraints

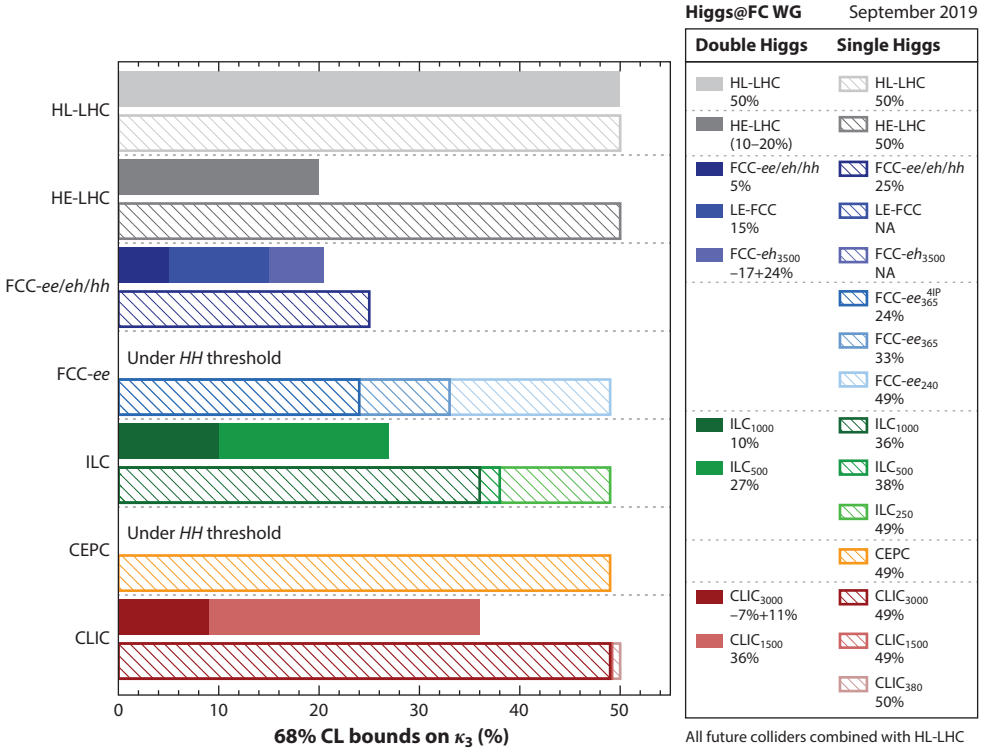


**Figure 6**

Expected precision on $\kappa_\lambda$ at different future collider scenarios. All results are shown in combination with the HL-LHC extrapolations from Reference 113 (*top line*). For each future collider, the constraints on $\kappa_\lambda$ obtained from *HH* and single-*H* measurements are shown separately, and the numerical values are given in the legend. A naïve combination of more recent extrapolations from ATLAS (118) and CMS (122) indicates that the precision within reach at the HL-LHC can be reduced from 50% (as in the figure) to ∼35%. Figure adapted from Reference 112 (CC BY 4.0).

on the quartic coupling strength, $\lambda_{HHHH}$, will likely be possible only via precision measurements of single- and double-Higgs production by exploiting information about NNLO and NLO EW corrections, respectively. The most promising option for direct measurements of the triple-Higgs process is a multi-TeV muon collider (124).

## 6. CONCLUSION

This review has explored the multifaceted aspects of *HH* production, delving into both the theoretical frameworks and the experimental efforts at the LHC. The future of *HH* production research stands at a pivotal point, with the potential to shed light on the profound mysteries of the Higgs mechanism and EW symmetry breaking and to reveal new facets of particle physics. The pursuit of the Higgs self-coupling requires careful consideration of the production and decay modes of *HH*, with different channels contributing to different aspects of the overall physics program. While direct production modes offer distinct signatures and insights, precision measurements of single-Higgs processes offer a complementary way to understand the Higgs self-interaction via loop processes. We have highlighted the critical role of advanced experimental techniques and the unique challenges presented by the main decay channels, as well as the

importance of pushing the experimental boundaries of the mass and momentum regimes explored. The insights gained from these searches not only enrich our understanding of the Higgs boson but also open avenues to probe BSM physics. As we look forward to LHC Run 3, the larger data set and planned experimental improvements promise to amplify our capabilities to illuminate the enigma of the Higgs potential and unlock new vistas in our understanding of the Universe.

## DISCLOSURE STATEMENT

The authors are not aware of any affiliations, memberships, funding, or financial holdings that might be perceived as affecting the objectivity of this review.

## ACKNOWLEDGMENTS

We gratefully acknowledge the US Department of Energy for financial support, as well Brown University (to L.G.) and Southern Methodist University (to K.J.C.L.). We also thank the LHC, ATLAS, and CMS Collaborations for all of the work and support that enabled the *HH* results and planned improvements that are summarized in this article.

## LITERATURE CITED

1. Englert F, Brout R. *Phys. Rev. Lett.* 13:321 (1964)
2. Higgs PW. *Phys. Lett.* 12:132 (1964)
3. Higgs PW. *Phys. Rev. Lett.* 13:508 (1964)
4. Aad G, et al. (ATLAS Collab.) *J. Instrum.* 3:S08003 (2008)
5. Chatrchyan S, et al. (CMS Collab.) *J. Instrum.* 3:S08004 (2008)
6. Aad G, et al. (ATLAS Collab.) *Phys. Lett. B* 716(1):1 (2012)
7. Chatrchyan S, et al. (CMS Collab.) *J. High Energy Phys.* 06:081 (2013)
8. Aad G, et al. (ATLAS Collab.) *J. High Energy Phys.* 04:117 (2015)
9. Sirunyan AM, et al. (CMS Collab.) *Phys. Lett. B* 779:283 (2018)
10. Aaboud M, et al. (ATLAS Collab.) *Phys. Lett. B* 786:59 (2018)
11. Sirunyan AM, et al. (CMS Collab.) *Phys. Rev. Lett.* 121:121801 (2018)
12. Aaboud M, et al. (ATLAS Collab.) *Phys. Lett. B* 784:173 (2018)
13. Sirunyan AM, et al. (CMS Collab.) *Phys. Rev. Lett.* 120:231801 (2018)
14. Aad G, et al. (ATLAS Collab.) *Eur. Phys. J. C* 82:717 (2022)
15. Tumasyan A, et al. (CMS Collab.) *Phys. Rev. Lett.* 131:061801 (2023)
16. Tumasyan A, et al. (CMS Collab.) *Phys. Lett. B* 846:137783 (2023)
17. Horn B. *Physics* 2:503 (2020)
18. Weir DJ. *Proc. Sci.* CHARGED2018:027 (2019)
19. Hamada Y, Kawai H, Oda K, Park SC. *Phys. Rev. D* 91:053008 (2015)
20. Reichert M, et al. *Phys. Rev. D* 97:075008 (2018)
21. Markkanen T, Rajantie A, Stopyra S. *Front. Astron. Space Sci.* 5:40 (2018)
22. Alison J, et al. *Rev. Phys.* 5:100045 (2020)
23. Dawson S, Dittmaier S, Spira M. *Phys. Rev. D* 58:115012 (1998)
24. Borowka S, et al. *Phys. Rev. Lett.* 117:012001 (2016); Erratum. *Phys. Rev. Lett.* 117:079901 (2016)
25. Baglio J, et al. *Eur. Phys. J. C* 79(6):459 (2019)
26. de Florian D, Mazzitelli J. *Phys. Rev. Lett.* 111:201801 (2013)
27. Shao DY, Li CS, Li HT, Wang J. *J. High Energy Phys.* 07:169 (2013)
28. de Florian D, Mazzitelli J. *J. High Energy Phys.* 09:053 (2015)
29. Grazzini M, et al. *J. High Energy Phys.* 05:059 (2018)
30. Aad G, et al. (ATLAS Collab.) *Phys. Lett. B* 800:135103 (2020)
31. Aad G, et al. (ATLAS Collab.) *Eur. Phys. J. C* 83(6):519 (2023)
32. CMS Collab. Tech. Rep. CMS-PAS-HIG-22-006, CERN, Geneva (2023)

33. Baglio J, et al. *Phys. Rev. D* 103:056002 (2021)
34. Bagnaschi E, Degrassi G, Gröber R. *Eur. Phys. J. C* 83:1054 (2023)
35. Heinrich G, Lang J, Scyboz L. *J. High Energy Phys.* 10:086 (2023)
36. Degrassi G, Giardino PP, Maltoni F, Pagani D. *J. High Energy Phys.* 10:080 (2016)
37. Maltoni F, Pagani D, Shivaji A, Zhao X. *Eur. Phys. J. C* 77:12 (2017)
38. Di Vita S, et al. *J. High Energy Phys.* 09:069 (2017)
39. Gorbahn M, Haisch U. *J. High Energy Phys.* 10:094 (2016)
40. Bizon W, Gorbahn M, Haisch U, Zanderighi G. *J. High Energy Phys.* 05:111 (2017)
41. McCullough M. *Phys. Rev. D* 90:015001 (2014)
42. Tumasyan A, et al. (CMS Collab.) *J. High Energy Phys.* 07:092 (2023)
43. Branco GC, et al. *Phys. Rep.* 516(1):1 (2012)
44. Randall L, Sundrum R. *Phys. Rev. Lett.* 83(17):3370 (1999)
45. Agashe K, Davoudiasl H, Perez G, Soni A. *Phys. Rev. D* 76:036006 (2007)
46. Fitzpatrick L, Kaplan J, Randall L, Wang L-T. *J. High Energy Phys.* 09:013 (2007)
47. Dugan MJ, Georgi H, Kaplan DB. *Nucl. Phys. B* 254:299 (1985)
48. Agashe K, Contino R, Pomarol A. *Nucl. Phys. B* 719(1/2):165 (2005)
49. Gildener E, Weinberg S. *Phys. Rev. D* 13:3333 (1976)
50. Alonso R, et al. *Phys. Lett. B* 722:330
51. Grzadkowski B, Iskrzyński M, Misiak M, Rosiek J. *J. High Energy Phys.* 2010:85 (2010)
52. Buchmüller W, Wyler D. *Nucl. Phys. B* 268(3):621 (1986)
53. Leung CN, Love ST, Rao S. *Z. Phys. C* 31:433 (1986)
54. Aad G, et al. (ATLAS Collab.) *Phys. Lett. B* 843:137880 (2023)
55. Sirunyan AM, et al. (CMS Collab.) *Eur. Phys. J. C* 81(6):488 (2021)
56. Aad G, et al. (ATLAS Collab.) *Phys. Lett. B* 847:138315 (2023)
57. Tumasyan A, et al. (CMS Collab.) *J. High Energy Phys.* 07:091 (2023)
58. Cacciari M, Salam GP, Soyez G. *J. High Energy Phys.* 04:063 (2008)
59. Ellis SD, Vermilion CK, Walsh JR. *Phys. Rev. D* 81:094023 (2010)
60. Larkoski AJ, Marzani S, Soyez G, Thaler J. *J. High Energy Phys.* 05:146 (2014)
61. Aad G, et al. (ATLAS Collab.) *Eur. Phys. J. C* 83(7):681 (2023)
62. Sirunyan AM, et al. (CMS Collab.) *J. Instrum.* 13:P05011 (2018)
63. Bols E, et al. *J. Instrum.* 15:P12012 (2020)
64. CMS Collab. Tech. Rep. CMS-PAS-BTV-22-001, CERN, Geneva (2023)
65. Qu H, Gouskos L. *Phys. Rev. D* 101:056019 (2020)
66. Tumasyan A, et al. (CMS Collab.) *J. Instrum.* 17:P07023 (2022)
67. Aad G, et al. (ATLAS Collab.) *J. High Energy Phys.* 01:069 (2015)
68. Sirunyan AM, et al. (CMS Collab.) *Comput. Softw. Big Sci.* 4(1):10 (2020)
69. CMS Collab. Tech. Rep. CMS-DP-2021-017, CERN, Geneva (2021)
70. ATLAS Collab. Tech. Rep. ATL-PHYS-PUB-2015-045, CERN, Geneva (2015)
71. ATLAS Collab. Tech. Rep. ATL-PHYS-PUB-2019-033, CERN, Geneva (2019)
72. Aad G, et al. (ATLAS Collab.) *J. High Energy Phys.* 11:163 (2020)
73. CMS Collab. Tech. Rep. CMS-DP-2016-038, CERN, Geneva (2016)
74. Aad G, et al. (ATLAS Collab.) *Phys. Rev. D* 108:052003 (2023)
75. Aad G, et al. (ATLAS Collab.) *J. High Energy Phys.* 07:108 (2020); Erratum. *J. High Energy Phys.* 01:145 (2021); Erratum. *J. High Energy Phys.* 05:207 (2021)
76. Tumasyan A, et al. (CMS Collab.) *Phys. Rev. Lett.* 129:081802 (2022)
77. Tumasyan A, et al. (CMS Collab.) *Phys. Rev. Lett.* 131:041803 (2023)
78. Junk T. *Nucl. Instrum. Methods A* 434:435 (1999)
79. Read AL. *J. Phys. G* 28:2693 (2002)
80. Cowan G, Cranmer K, Gross E, Vitells O. *Eur. Phys. J. C* 71:1554 (2011); Erratum. *Eur. Phys. J. C* 73:2501 (2013)
81. Kotthoff L, Wahab H, Johnson P. arXiv:2108.00002 [cond-mat.mtrl-sci] (2021)
82. David A, et al. (LHC Higgs Cross Sect. Work. Group.) arXiv:1209.0040 [hep-ph] (2012)

83. Andersen JR, et al. (LHC Higgs Cross Sect. Work. Group.) arXiv:1307.1347 [hep-ph] (2013)
84. Aad G, et al. (ATLAS Collab.) *J. High Energy Phys.* 07:040 (2023)
85. Tumasyan A, et al. (CMS Collab.) *Phys. Lett. B* 842:137531 (2023)
86. Elagin A, Murat P, Pranko A, Safonov A. *Nucl. Instrum. Methods A* 654:481 (2011)
87. Bianchini L, Conway J, Friis EK, Veelken C. *J. Phys. Conf. Ser.* 513:022035 (2014)
88. ATLAS Collab. *Plots for Higgs 2023*. Data Vis., CERN, Geneva. **https://twiki.cern.ch/twiki/bin/view/AtlasPublic/TauTriggerPublicResults#Plots_for_Higgs_2023** (2023)
89. CMS Collab. Tech. Rep. CMS-DP-2023-050, CERN, Geneva (2023)
90. Aad G, et al. (ATLAS Collab.) arXiv:2310.12301 [hep-ex] (2023)
91. Sirunyan AM, et al. (CMS Collab.) *J. High Energy Phys.* 2103:257 (2020)
92. Aaboud M, et al. (ATLAS Collab.) *J. High Energy Phys.* 04:092 (2019)
93. Aaboud M, et al. (ATLAS Collab.) *J. High Energy Phys.* 05:124 (2019)
94. Aaboud M, et al. (ATLAS Collab.) *Eur. Phys. J. C* 78(12):1007 (2018)
95. Aad G, et al. (ATLAS Collab.) *Phys. Lett. B* 801:135145 (2020)
96. Tumasyan A, et al. (CMS Collab.) *J. High Energy Phys.* 07:095 (2023)
97. Sirunyan AM, et al. (CMS Collab.) *J. High Energy Phys.* 01:054 (2018)
98. Tumasyan A, et al. (CMS Collab.) *J. High Energy Phys.* 06:130 (2023)
99. Aad G, et al. (ATLAS Collab.) *Phys. Lett. B* 843:137745 (2023)
100. Aad G, et al. (ATLAS Collab.) *J. High Energy Phys.* 02:037 (2024)
101. Aad G, et al. (ATLAS Collab.) *Phys. Rev. D* 106:052001 (2022)
102. Aad G, et al. (ATLAS Collab.) *J. High Energy Phys.* 01:066 (2024)
103. Tumasyan A, et al. (CMS Collab.) *Nature* 607:60 (2022)
104. Branco GC, et al. *Phys. Rep.* 516:1 (2012)
105. Drozd A, Grzadkowski B, Gunion J, Jiang Y. *J. High Energy Phys.* 11:105 (2014)
106. Robens T. *Symmetry* 15:27 (2023)
107. Ellwanger U, Hugonie C, Teixeira AM. *Phys. Rep.* 496:1 (2010)
108. Maniatis M. *Int. J. Mod. Phys. A* 25:3505 (2010)
109. Carena M, et al. *Phys. Rev. D* 93:035013 (2016)
110. Aad G, et al. (ATLAS Collab.) *Phys. Rev. Lett.* 132:021803 (2024)
111. Hayrapetyan A, et al. (CMS Collab.) arXiv:2403.16926 [hep-ex] (2024)
112. Ellis RK, et al. arXiv:1910.11775 [hep-ex] (2019)
113. Cepeda M, et al. (Phys. HL-LHC Work. Group Collab.) arXiv:1902.00134 (2018)
114. ATLAS Collab. Tech. Rep. ATL-PHYS-PUB-2015-046, CERN, Geneva (2015)
115. ATLAS Collab. Tech. Rep. ATL-PHYS-PUB-2022-001, CERN, Geneva (2022)
116. Sirunyan AM, et al. (CMS Collab.) *Phys. Rev. Lett.* 122:121803 (2019)
117. Dawson S, et al. arXiv:2209.07510 [hep-ph] (2022)
118. ATLAS Collab. Tech. Rep. ATLAS-CONF-2023-053, CERN, Geneva (2022)
119. CMS Collab. Tech. Rep. CMS-PAS-FTR-21-004, CERN, Geneva (2022)
120. ATLAS Collab. Tech. Rep. ATL-PHYS-PUB-2021-044, CERN, Geneva (2021)
121. CMS Collab. Tech. Rep. CMS-PAS-FTR-21-003, CERN, Geneva (2022)
122. ATLAS Collab., CMS Collab. White Pap. ATL-PHYS-PUB-2022-018, CERN, Geneva (2022)
123. de Florian D, Fabre I, Mazzitelli J. *J. High Energy Phys.* 03:155 (2020)
124. Chiesa M, et al. *J. High Energy Phys.* 09:098 (2020)
125. Sirunyan AM, et al. (CMS Collab.) *J. Instrum.* 13:P10005 (2018)